JGR Solid Earth

RESEARCH ARTICLE
10.1029/2018JB016982

Depth Determination of the 2010 El Mayor-Cucapah Earthquake Sequence ($M \geq 4.0$)

Chunquan Yu[1,2], Egill Hauksson[1], Zhongwen Zhan[1], Elizabeth S. Cochran[3], and Donald V. Helmberger[1]

[1]Seismological Laboratory, California Institute of Technology, Pasadena, CA, USA, [2]Department of Earth and Space Sciences, Southern University of Science and Technology, Shenzhen, Guangdong, China, [3]Earthquake Science Center, U. S. Geological Survey, Pasadena, CA, USA

Key Points:
- We determine earthquake depths of the 2010 El Mayor-Cucapah sequence by modeling *Pn* depth phases and using a relative location method
- The 2010 El Mayor-Cucapah earthquake sequence is mainly confined in the depth range between 3 and 10 km
- Most aftershocks are located outside or near the lower terminus of coseismic high-slip patches of the main shock

Supporting Information:
- Supporting Information S1
- Table S1

Correspondence to:
C. Yu,
yucq@sustech.edu.cn

Citation:
Yu, C., Hauksson, E., Zhan, Z., Cochran, E. S., & Helmberger, D. V. (2019). Depth determination of the 2010 El Mayor-Cucapah earthquake sequence ($M \geq 4.0$). *Journal of Geophysical Research: Solid Earth*, *124*, 6801–6814. https://doi.org/10.1029/2018JB016982

Received 3 NOV 2018
Accepted 22 JUN 2019
Accepted article online 2 JUL 2019
Published online 12 JUL 2019

Abstract The 2010 M_W 7.2 El Mayor-Cucapah earthquake ruptured a zone of ~120 km in length in northern Baja California. The geographic distribution of this earthquake sequence was well constrained by waveform relocation. The depth distribution, however, was poorly determined as it is near the edge of, or outside, the Southern California Seismic Network. Here we use two complementary methods to constrain the focal depths of moderate-sized events ($M \geq 4.0$) in this sequence. We first determine the absolute earthquake depth by modeling the regional depth phases at high frequencies (~1 Hz). We mainly focus on *Pn* and its depth phases *pPn* and *sPn*, which arrive early at regional distance and are less contaminated by crustal multiples. To facilitate depth phase identification and to improve signal-to-noise ratio, we take advantage of the dense Southern California Seismic Network and use array analysis to align and stack *Pn* waveforms. For events without clear depth phases, we further determine their relative depths with respect to those with known depths using differential travel times of the *Pn*, direct *P*, and direct *S* phases recorded for event pairs. Focal depths of 93 out of 122 $M \geq 4.0$ events are tightly constrained with absolute uncertainty of about 1 km. Aftershocks are clustered in the depth range of 3–10 km, suggesting a relatively shallow seismogenic zone, consistent with high surface heat flow in this region. Most aftershocks are located outside or near the lower terminus of coseismic high-slip patches of the main shock, which may be governed by residual strains, local stress concentration, or postseismic slip.

1. Introduction

Earthquake focal depth is a key parameter in earthquake seismology. Knowledge of earthquake depth is important to reveal the geometry of Earth's internal structures (e.g., Brudzinski et al., 2007; Engdahl et al., 1998; Hauksson, 2000); to understand the thermal, rheological, and lithological properties of the lithosphere (e.g., Chen & Molnar, 1983; Prieto et al., 2017); and to infer the deformation history of rock materials (e.g., Sibson, 1986). Earthquake depth also has a strong effect on ground motions (e.g., Lui et al., 2016) and thus is crucial for seismic hazard assessment.

Routine determination of earthquake depth relies on the travel times of major body-wave phases. Yet due to its tradeoff with earthquake origin time and inaccurate three-dimensional Earth structure, precise earthquake depth can be difficult to obtain. Previously, it has been suggested that good constraint on earthquake depth requires at least one nearby station, whose distance from the epicenter is on the same order as the focal depth (Gomberg et al., 1990). Globally, earthquake depth can be significantly improved if teleseismic depth phases, such as *pP* and *sP* (reflections from the Earth's solid surface near the source) and *pwP* (water surface reflection), are identified and included in the relocation procedure (e.g., Engdahl et al., 1998). However, such practice is usually limited to large-magnitude earthquakes, such as $M \geq 5.2$ (Engdahl et al., 1998). Moderate-to-small magnitude earthquakes (e.g., $M < 5$) are usually recorded regionally, although some studies analyzed teleseismic waveforms for *M*4.5+ events (e.g., Craig & Heyburn, 2015).

The 2010 El Mayor-Cucapah earthquake sequence is a typical example of a sequence in which focal depths are poorly determined, which prevents detailed understanding of seismotectonics around the U.S.-Mexico border of the Pacific-North America plate boundary (Hauksson et al., 2011). Most events in this sequence occurred near the edge of, or outside, the dense Caltech/U.S. Geological Survey (USGS) Southern California Seismic Network (SCSN; Figure 1). As the distances between events and stations increase, both the availability of arrival time picks and reliability of estimated focal depths decrease. In the southern part

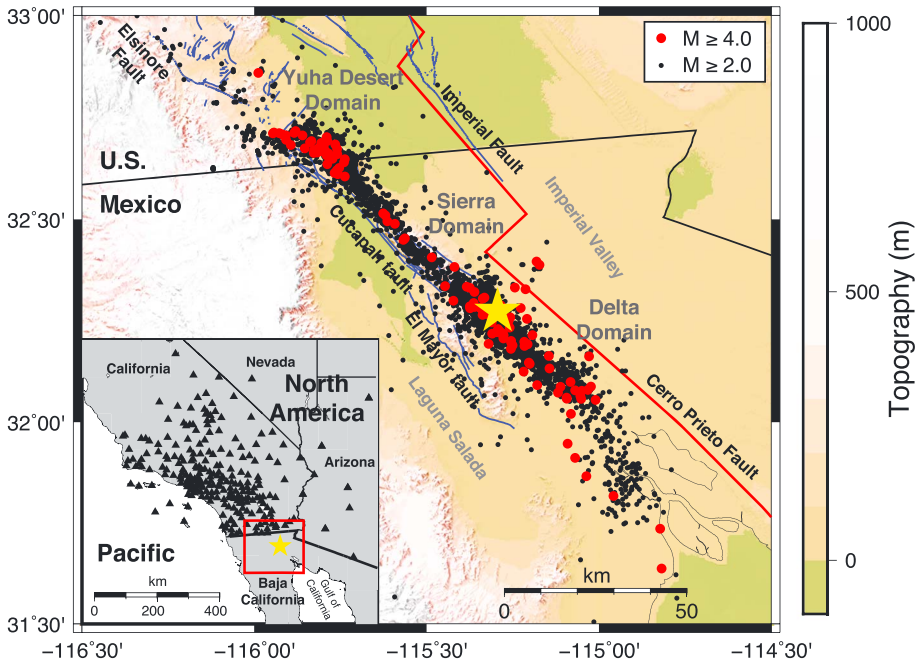

Figure 1. Map showing the spatial distribution of the 2010 El Mayor-Cucapah earthquake sequence. Yellow star is the main shock. Red and black dots are events with $M \geq 4.0$ and $M \geq 2.0$, respectively. Geological surveys suggest three domains of the surface rupture, including the Yuha Desert domain, the Sierra domain, and the Delta domain (Fletcher et al., 2014). Inset in the lower left shows the distribution of the Southern California Seismic Network.

of this earthquake sequence, there are almost no nearby stations and minimal depth constraints (Hauksson et al., 2011).

A few methods have been proposed to constrain depths of regional earthquakes. Spectral ratios between surface waves and body waves have sometimes been used as a depth discriminant since the excitation of surface waves relies on the depth of earthquakes (e.g., Kafka, 1990; Langston, 1987; Tibi et al., 2018; Tsai & Aki, 1970). Yet, the sensitivity of surface waves to focal depth decreases significantly with focal depth, so that such methods may be more useful for analyzing shallow focus earthquakes. Amplitude spectra of surface waves can also be used to determine focal depth (Jia et al., 2017). However, focal mechanism, local velocity, and attenuation structures potentially have strong source and path effects on the amplitude and spectrum of surface waves (Jia et al., 2017). To this end, depth determination using surface waves can have large uncertainties.

Similar to teleseismic earthquakes, tight constraint on regional earthquake depth can be obtained using regional depth phases. Because differential travel times between regional depth phases and their reference phases are most sensitive to the local structure above the hypocenter, uncertainty in estimated focal depth is on the same order as that of the velocity model. Previous studies have used various regional depth phases to determine focal depth, including depth phases of the direct *P* phase at small epicentral distance, for example, <100 km (e.g., Langston, 1987; Ma, 2010; Wang et al., 2011), depth phases of *PmP* and *SmS* (*P* and *S* wave reflections from the top of the Moho) at slightly larger distance, for example, 100–300 km (e.g., Helmberger et al., 1992; Ma, 2010), and depth phases of *Pn* (*P* wave bottoming in the uppermost mantle) at even larger distance, for example, >200 km (e.g., Husebye et al., 2013; Zonno & Kind, 1984). A major challenge of using regional depth phases comes from the complexity of regional waveforms. The amplitude of depth phases is modulated by the earthquake focal mechanism, and the arrival of depth phases can be obscured by other crustal phases. As a result, depth phases can be difficult to identify using data from sparse seismic stations (Husebye et al., 2013).

Here we study the depth distribution of the 2010 El Mayor-Cucapah earthquake sequence. We take advantage of the dense distribution of SCSN and use array analysis to help identify regional depth phases and to enhance their signal-to-noise ratio. We focus on events with $M \geq 4.0$, as their signal-to-noise ratio is

higher and the number of events is large enough to characterize the spatial distribution of this earthquake sequence. We use *Pn* and its depth phases and apply waveform modeling to determine absolute earthquake depths. For events without clear *Pn* depth phases, we further determine their relative depth with respect to those well-determined ones using differential travel times of *Pn*, *P*, and *S*.

2. Data and Methods

2.1. The 2010 El Mayor-Cucapah Earthquake Sequence

The 2010 M_W 7.2 El Mayor Cucapah earthquake occurred near the boundary between the Pacific plate and the North American plate (Figure 1). It released some of the accumulated right-lateral shear between the two plates and revealed a complex fault system (Fletcher et al., 2014; Hauksson et al., 2011). The main shock was initiated on a small extensional fault and then propagated bilaterally along two major segments (Wei et al., 2011). The NW and SE segments, dipping in opposite directions, end near the U.S.-Mexico international border and the northern tip of the Gulf of Mexico, respectively. There are three major domains of the surface rupture, which include Yuha Desert domain in the north, Sierra domain in the middle, and Delta domain in the south (Fletcher et al., 2014). The total rupture zone is about 120 km in length (Wei et al., 2011).

By the end of 2010, the SCSN detected ~20,000 earthquakes associated with the 2010 El Mayor-Cucapah sequence. Among them, there are 122 earthquakes with $M \geq 4.0$ (including three foreshocks in 2010). These events were routinely relocated using the double-difference algorithm (Hauksson et al., 2011), and their geographic distribution was well constrained. Aftershocks are widely spread along the main shock rupture zone, but there are two main clusters: one near the epicenter of the main shock and the other near the northern end of the rupture zone (or the Yuha Desert; Figure 1). Earthquake depths in the Yuha Desert are relatively well constrained as there are a few nearby SCSN stations. A local temporary seismic network was also used for more detailed earthquake relocation (Kroll et al., 2013; Ross et al., 2017). However, as distance to the SCSN increases, there is almost no depth constraint for events to the south (Hauksson et al., 2011).

2.2. *Pn* and Its Depth Phases

We use regional *Pn* depth phases to constrain the absolute depth of the 2010 El Mayor-Cucapah earthquake sequence. This earthquake sequence is relatively far away from SCSN, especially for events that occurred in the southern part of the rupture, so that *Pn* phase is often the first arrival (crossover distance about 1°). For a layered crust, the depth phases *pPn* and *sPn* share similar ray paths with *Pn* except near the source region (Figure 2a). The *sPn* (*pPn*) phase travels upward from the hypocenter as an *S* wave (*P* wave). It undergoes *S*-to-*P* (*P*-to-*P*) reflection at the free surface and then propagates as a *Pn* wave to the station. The differential travel times between *Pn* and its depth phases, which do not vary with epicentral distance, are most sensitive to the focal depth and the velocity structure above the source.

The principle of using *Pn* and its depth phases to determine earthquake depth is illustrated in Figure 2. The differential time between *sPn* (*pPn*) and *Pn* for a layered crust can be expressed as

$$T_{sPn-Pn} = \int_0^H \left(\sqrt{V_P^{-2} - p_{Pn}^2} + \sqrt{V_S^{-2} - p_{Pn}^2} \right) \mathrm{d}z \tag{1}$$

$$T_{pPn-Pn} = 2\int_0^H \sqrt{V_P^{-2} - p_{Pn}^2}\,\mathrm{d}z \tag{2}$$

where H is the focal depth and V_P and V_S are *P* and *S* wave speeds, respectively. p_{Pn} is a constant equal to the inverse of the upper mantle *P* wave speed and is the ray parameter of *Pn*, *pPn*, and *sPn*. Given *P* and *S* wave speeds above the hypocenter, earthquake depth can be uniquely determined through equations (1) or (2) if T_{sPn-Pn} or T_{pPn-Pn} is measured.

Figure 2b shows synthetic *Pn* waveforms as a function of earthquake focal depth. We assume a velocity model with a 22-km-thick crust overlying a half-space mantle. Crustal *P* wave speed is 6.4 km/s. V_P/V_S ratio is fixed at 1.8. A strike-slip focal mechanism, which is typical for events in the Pacific-North America plate boundary, is used for the synthetic calculation. All synthetic waveforms in this study are calculated using the frequency-wavenumber method (Zhu & Rivera, 2002). To avoid contamination from other crustal phases, such as direct *P* and *PmP* (Figure 2a), we set a station-event distance at 500 km. It is clear that the

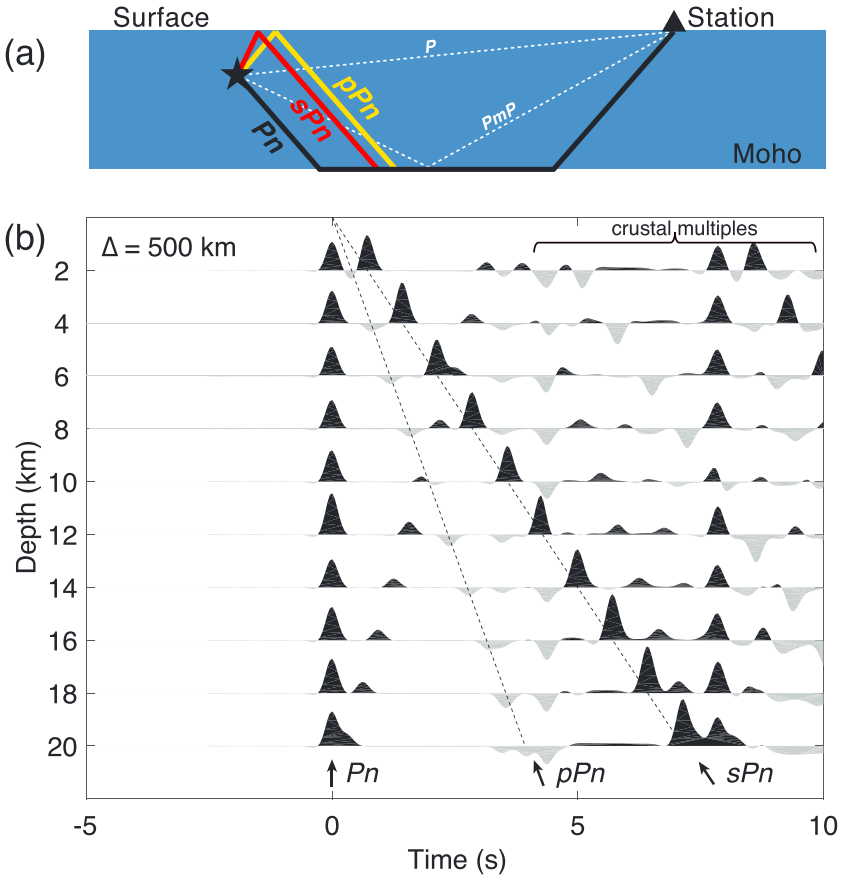

Figure 2. (a) Schematic diagram showing ray paths of *Pn* and its depth phases. Thin dashed lines are ray paths of direct *P* and *PmP*. (b) Synthetic *Pn* waveforms as a function of earthquake depth. The source-receiver distance is fixed at 500 km to minimize interference from other crustal phases, such as direct *P* and *PmP*. Waveforms are aligned by the maximum peak of *Pn*. A simple one-layered crustal model and a strike-slip focal mechanism are used.

differential travel times between *Pn* and its depth phases increase almost linearly with focal depth (Figure 2b).

The amplitudes of *Pn* and its depth phases are modulated by the earthquake focal mechanism. In order to use waveform modeling to fit observed amplitudes and arrival times of *Pn* depth phases, we first determine focal mechanisms of $M \geq 4.0$ events in the 2010 El Mayor-Cucapah earthquake sequence.

2.3. Focal Mechanisms of the 2010 El Mayor-Cucapah Earthquake Sequence

We determine earthquake focal mechanisms using the Cut-and-Paste method (Zhu & Helmberger, 1996). We first remove instrument response for each station and rotate three-component velocity seismograms into vertical, radial, and tangential components. We then apply a 10–50-s bandpass filter to the waveforms and cut them into *Pnl* (Helmberger & Engen, 1980) and surface wave segments. Traces of low quality, either low signal-to-noise ratio or abnormal amplitudes, are discarded before being inverted for the focal mechanism. Synthetic waveforms are calculated using a simple 1-D velocity model with a 22-km-thick crust (Hauksson, 2000). We note that our estimated focal mechanisms are generally insensitive to the assumed velocity model as the inversion procedure allows for time shifts of each segment. The Cut-and-Paste method has also been used to estimate earthquake depth in other studies (e.g., Zhu & Helmberger, 1996). However, we do not find that the depth estimates are well constrained in this study. Our study region is characterized by complex 3-D velocity structures, including strong lateral heterogeneities and shallow sedimentary basins (Fletcher et al., 2014). In addition, most seismic stations are located to the north and northwest direction of the earthquake source region, and thus, azimuthal coverage is not ideal (Figure 1). As a result, the misfit

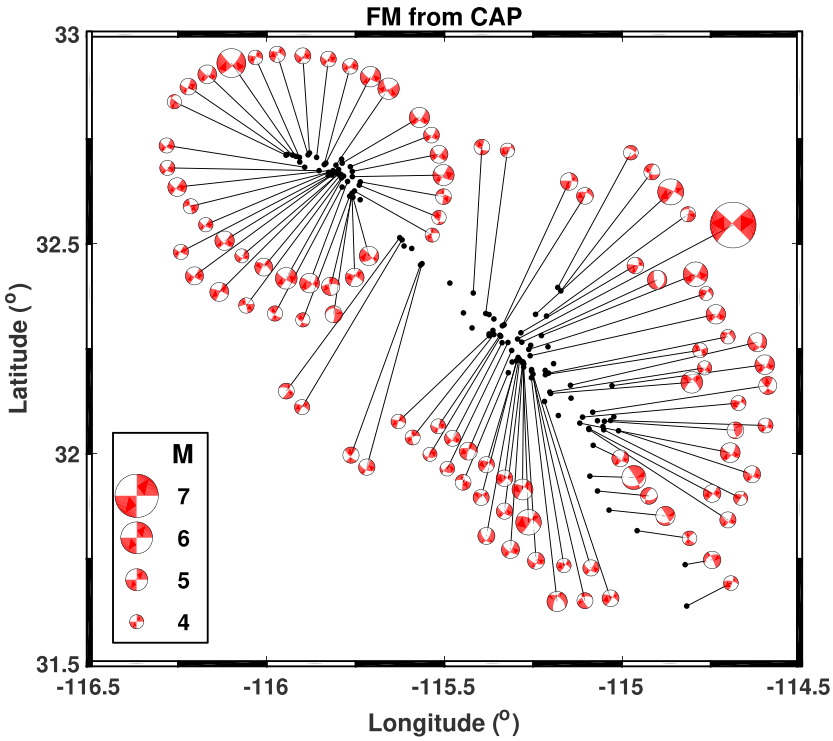

Figure 3. Focal mechanisms (FM) for $M \geq 4.0$ events of the 2010 El Mayor-Cucapah earthquake sequence. These focal mechanisms are inverted with the Cut-and-Paste method (CAP; Zhu & Helmberger, 1996) except for the main shock that is from the global CMT solution.

function does not always have a concave shape along the depth axis, and even if it has, its global minimum may vary for different velocity models, such as with and without shallow sediments (supporting information Figure S1). In contrast, the estimated focal mechanisms are often stable over a wide depth range.

The 2010 El Mayor-Cucapah sequence is dominated by strike slip focal mechanisms (Figure 3), similar to those reported previously (Hauksson et al., 2011). Many events occurred on the northwest to west-northwest-striking faults as can be inferred from the geographic distribution of background seismicity (Figure 1). In the Yuha Desert, focal mechanisms show great consistency among different events. However, there is a conjugate pattern of faulting with both northwest and northeast directions (Kroll et al., 2013). Focal mechanism uncertainties generally increase southward as event-station distance increases and azimuthal coverage narrows. The focal mechanism of the main shock is directly adopted from the global CMT catalog (Ekström et al., 2012). Detailed focal mechanism parameters are shown in Table S1.

2.4. Absolute Depth Determination by Modeling *Pn* Depth Phases

To facilitate regional depth phase identification, we take advantage of the dense station distribution of SCSN and check the consistency of *Pn* waveforms for stations in a narrow azimuthal range. Since *Pn* and its depth phases share similar ray paths near the receiver, their relative amplitude and arrival time should be independent of epicentral distance. Other crustal phases, such as direct *P* and *PmP*, whose slownesses are different from *Pn* and its depth phases, can thus be distinguished. We bandpass filter *Pn* velocity seismograms between 0.5 and 2 Hz (optimal for most events) and only select traces with clear *Pn* depth phases. Waveforms within a narrow azimuthal range are further stacked to enhance the signal-to-noise ratio.

The amplitudes of depth phases are sensitive to the focal mechanism. We use inverted focal mechanisms (Table S1) to model regional *Pn* depth phases. To account for inversion uncertainties, we also search for other possible focal mechanism solutions (which give similar misfit reductions), if necessary, to better fit the phase and amplitude of depth phases. Conversely, the amplitude of depth phases can potentially be used in conjunction with conventional methods, such as the Cut-and-Paste (Zhu & Helmberger, 1996), to more

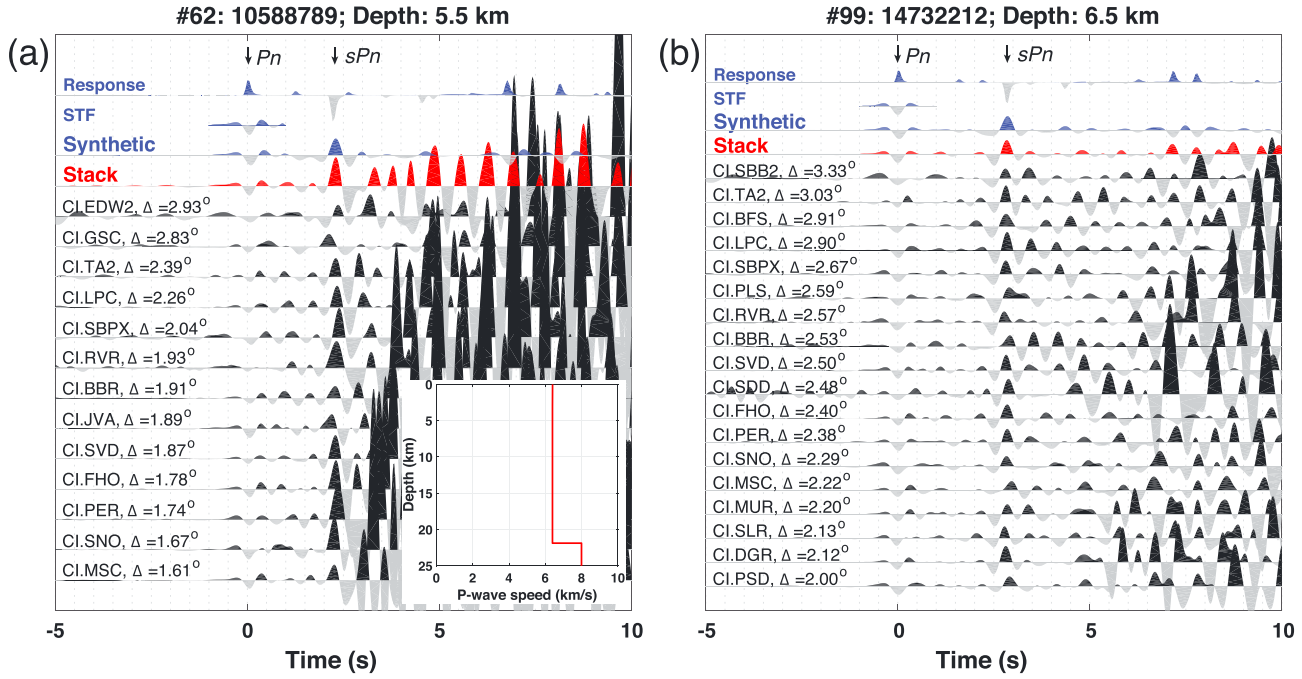

Figure 4. Examples of *Pn* depth phase modeling. (a) and (b) are for events located in the Yuha Desert and near the hypocenter of the main shock, respectively. Observed vertical-component waveforms (in ground velocity) are stacked (red trace) to enhance the signal-to-noise ratio of *Pn* and its depth phases. Synthetic waveforms are computed by convolving the Green's function (labeled "Response") with the *Pn* source wavelet (labeled STF). The latter is directly derived from the stacked waveform using a time window of [−1 1] s around the picked *Pn* phase. Inset in (a) shows the *P* wave velocity model used for waveform modeling.

tightly constrain the focal mechanism. However, this is beyond the scope of this paper but may be pursued as a future research direction.

Waveform complexity can arise when there are soft sediments near the surface (Helmberger et al., 1992; Mori, 1991). Thick, low-velocity sediments can have a strong effect on the amplitude of *Pn* depth phases by changing the *P*-to-*P* and *S*-to-*P* reflection coefficients. In general, the amplitudes of *pPn* and *sPn* are increased and decreased, respectively, compared with those from a model without sediments. For strike-slip focal mechanisms, our synthetic simulations suggest that when the sedimentary thickness is less than about 1 km, *sPn* is usually larger than *pPn* (supporting information Figure S2). However, *pPn* becomes stronger than *sPn* when the sediment is thick (>1 km) and of low velocity ($V_P < 3$ km/s).

The 2010 El Mayor-Cucapah earthquake sequence occurred near the edge of the Imperial Valley. The sedimentary layer in the source region is much thinner than that in the center of the Imperial Valley, where it can be as thick as ~5 km (e.g., Han et al., 2016; Persaud et al., 2016). Although the geological structure of this earthquake sequence is complex and lateral variable (Fletcher et al., 2014), we find that observed *Pn* depth phases can be well modeled with 1-D velocity models. For most events, *sPn* is stronger than *pPn*, suggesting that sedimentary effect is not significant near the source. Note, we do observe strong sedimentary effect for wave paths across the Imperial Valley, so we do not use these stations for *Pn* depth phase modeling (Yu et al., 2019). We use a 1-D crustal model with constant crustal velocity ($V_P = 6.4$ km/s and $V_P/V_S = 1.8$) to model *sPn* of these events. For events that occurred in the southern part of the Delta domain or near the center of the Imperial Valley, where sediments are thicker, we use a crustal model with 3-km-thick sediments (V_P increases linearly from 3 km/s at the free surface to 6.4 km/s at the bottom of the sediments; supporting information Figure S2) to model *pPn*.

Figure 4 shows an example of regional depth phase modeling for two different events: one in the Yuha Desert (Figure 4a) and the other near the hypocenter of the main shock (Figure 4b). Both events show clear *Pn* depth phases between 2 and 3 s, which are coherent among different stations. We use a one-layered crustal model to generate synthetic Green's functions at various focal depths. The source wavelet is directly estimated from the stacked *Pn* waveform using a [−1 1]-s time window around the *Pn* phase. Synthetic

waveforms (convolution of Green's functions and the source wavelet) are compared with the observation to determine the focal depth. Since the relative behavior between *Pn* and its depth phases does not change with distance, we fix the source-receiver distance at 500 km, which is larger than those of most recording stations. We do not try to model other crustal phases, such as direct *P* and *PmP* (e.g., Figure 4a). Finally, to account for lateral variations in velocity structure, we apply a time correction for the focal depth using the community velocity model CVM-S4.26 (Lee et al., 2014). A typical absolute depth uncertainty is ~0.5 km, assuming 5% uncertainty in *P* and *S* wave speed. The variation in depth estimates across the stations is less than 0.5 km, assuming a perturbation of 0.1 s in depth phase arrivals. Waveform modeling for events with identified *Pn* depth phases is shown in supporting information Figure S3.

2.5. Relative Depth Determination Using *Pn*, *P*, and *S* Differential Travel Times

Regional depth phases are sometimes difficult to identify for reasons including weak amplitudes related to the radiation pattern, structural complexities near the source, and interference by other crustal phases. For events without clear *Pn* depth phases, we determine their relative depths with respect to known ones (determined above) using differential travel times of *Pn*, direct *P*, and *S*. Compared with conventional relative location method using *P* and *S* differential times only, the incorporation of *Pn* differential times can significantly reduce the relative depth uncertainty, especially when stations are far away from the source.

If we consider a homogeneous velocity medium, the differential arrival time of *P* and *S* recorded at an arbitrary station for an event pair can be formulated as (source-receiver distance is much larger than intersource distance)

$$\Delta T_P = \Delta H \cdot \eta_P + \Delta X \cos(\varphi - \varphi_0) \cdot p_P + \Delta o \tag{3}$$

$$\Delta T_S = \Delta H \cdot \eta_S + \Delta X \cos(\varphi - \varphi_0) \cdot p_S + \Delta o \tag{4}$$

where for *P* and *S* waves, respectively, $p_P \left(= \frac{\sin\theta_P}{V_P}\right)$ and $p_S \left(= \frac{\sin\theta_S}{V_S}\right)$ are horizontal slownesses (or ray parameters), θ_P and θ_S are takeoff angles, $\eta_P \left(= \pm\sqrt{V_P^{-2} - p_P^2}\right)$ and $\eta_S \left(= \pm\sqrt{V_S^{-2} - p_S^2}\right)$ are vertical slownesses, and V_P and V_S are wave speed near the event pair. Polarities of η_P and η_S depend on whether rays travel upward (+) or downward (−) near the sources. ΔH and ΔX are the differences of depth and horizontal distance between the event pair. φ is the azimuth from the event pair center to the station (clockwise from north). φ_0 is the relative azimuth of the event pair. Δo is the differential origin time.

For stations at relatively large regional distances (compared with focal depth), the takeoff angle of both *P* and *S* waves are nearly horizontal. Thus, p_P and p_S are close to $\frac{1}{V_P}$ and $\frac{1}{V_S}$, respectively, and η_P and η_S are much smaller (close to zero). In other words, ΔH cannot be accurately determined using ΔT_P and ΔT_S only.

ΔH can be determined, however, if we consider *Pn* differential times (ΔT_{Pn})

$$\Delta T_{Pn} = -\Delta H \cdot \eta_{Pn} + \Delta X \cos(\varphi - \varphi_0) \cdot p_{Pn} + \Delta o \tag{5}$$

where $\eta_{Pn} \left(= \sqrt{V_P^{-2} - p_{Pn}^2}\right)$ is the vertical slowness of the *Pn* wave. The minus sign of the first term on the right-hand side is due to the downward going ray path of *Pn*.

To illustrate how we determine ΔH by combining measurements of ΔT_P, ΔT_S, and ΔT_{Pn}, we consider a simple case where stations are located at a constant distance from the event pair center and are uniformly distributed along azimuth (Figure 5). The two events are offset by 0.1° horizontally and 5 km vertically. Differential arrival times of ΔT_P, ΔT_S, and ΔT_{Pn} all show perfect sinusoid variations with respect to azimuth (Figure 5c). Assuming a V_P or V_S value near the event pair center, we can uniquely determine ΔX and φ_0 in equations (3)–(5) using any of these three curves. Once ΔX and φ_0 are determined, the azimuth-dependent term in equations (3)–(5) can be eliminated, the results of which will give constant values of $\overline{\Delta T_P}$, $\overline{\Delta T_S}$, and $\overline{\Delta T_{Pn}}$ (central lines in Figure 5c). ΔH can then be determined by taking the difference between $\overline{\Delta T_P}$ (or $\overline{\Delta T_S}$) and $\overline{\Delta T_{Pn}}$, which will further eliminate the Δo term, that is,

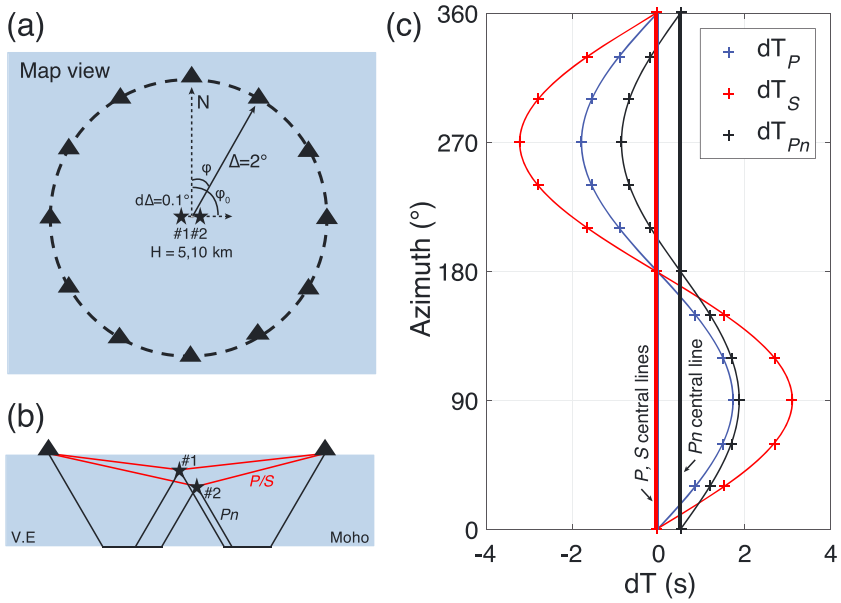

Figure 5. Illustration of relative depth determination using differential travel times of *Pn*, *P*, and *S*. (a) Map view showing distribution of an event pair and the recording stations. (b) Ray paths of *Pn*, *P*, and *S* in a vertical cross section. (c) Azimuthal variation of differential travel times between the event pair. Note that when stations are far away, the central lines of *P* and *S* are both near zero, suggesting that they are insensitive to focal depth. In contrast, the difference between the *Pn* central line and the *P* (or *S*) is most sensitive to the relative focal depth of the event pair.

$$\Delta H = \frac{\overline{\Delta T}_P - \overline{\Delta T_{Pn}}}{\eta_P + \eta_{Pn}} \tag{6}$$

or

$$\Delta H = \frac{\overline{\Delta T}_S - \overline{\Delta T_{Pn}}}{\eta_S + \eta_{Pn}} \tag{7}$$

In this study, we use events with known focal depths (determined above using *Pn* depth phase modeling) as master events. We form event pairs by searching for nearby events within a maximum horizontal distance of 20 km using the catalog locations (Hauksson et al., 2011). Figure 6 shows a typical example of an event pair where event 1 (#91 in Table S1) has and event 2 (#82 in Table S1) does not have clear *Pn* depth phases. We use an average crustal velocity model for the source region (Hauksson, 2000) and apply ray tracing to calculate the theoretical arrivals and horizontal and vertical slownesses for *Pn*, *P*, and *S* phases. We then extract *Pn*, *P*, and *S* waveforms using time windows of [−3, −1] s, [−1, 3] s, and [−1, 3] s around their theoretical arrival times, respectively. We use vertical component for *Pn* and *P* and tangential component for *S*. *Pn* is used only when it arrives at least 2 s before *P*, which corresponds to a minimum epicentral distance of about 150 km. These time windows contain the main energy from these phases and also minimize the interference from other phases. All waveforms are filtered in the frequency band between 0.5 and 2 Hz. We apply waveform cross correlation to derive differential arrival times of these phases. Only stations with high cross-correlation coefficients (>0.7) are retained (Figure 7).

For all event pairs with relatively good azimuthal coverage (azimuthal range > 90°), we then apply a grid search to determine their relative locations (latitude, longitude and depth) and origin time difference. *Pn*, *P*, and *S* traces are weighted by their waveform cross-correlation coefficients. We calculate the average arrival time misfit at each grid point using the *L*1 norm, which has been shown to be effective in obtaining accurate event locations (Shearer, 1997). Figure 8 shows the misfit distribution along four cross sections passing through the best-fit parameters. The minimum travel-time misfit is about 0.05 s. Event 1 is located to the northwest of event 2 (dlat = 0.05°, dlon = −0.06°), consistent with the relocated catalog of SCSN (dlat = 0.048°, dlon = −0.058°; Table S1). Event 1 is deeper than event 2 by 0.4 km, significantly

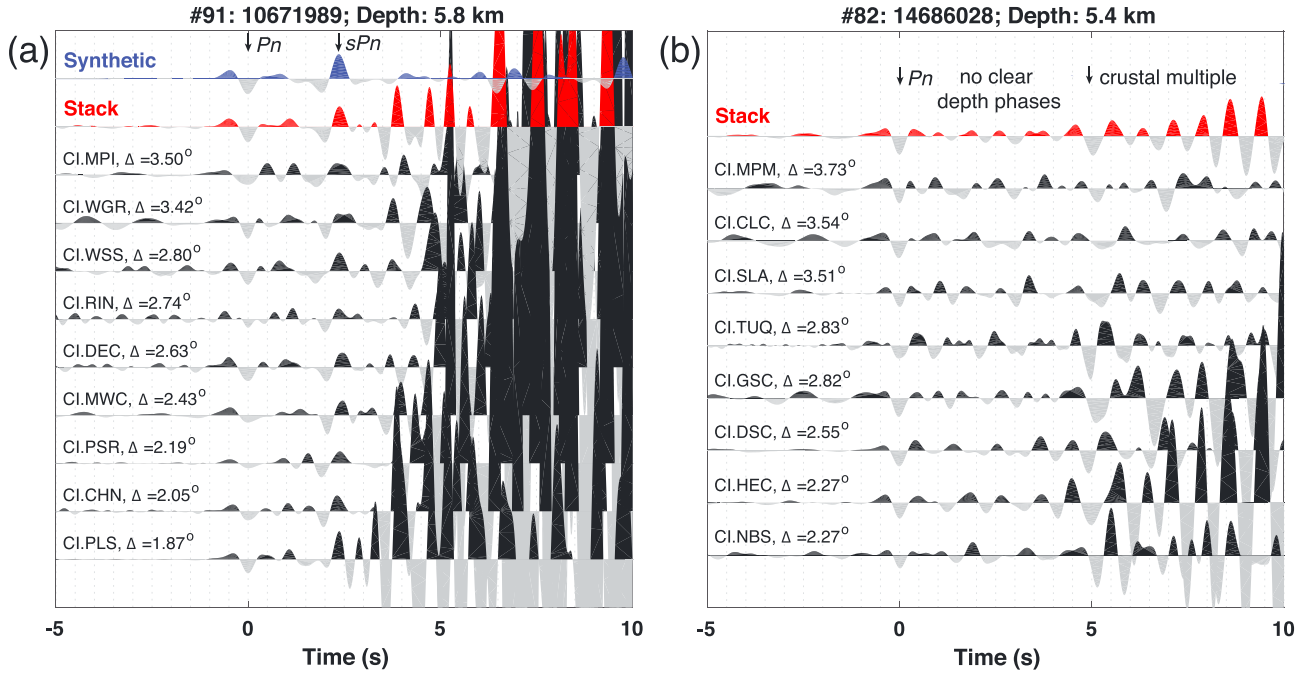

Figure 6. Example of an event pair where (a) event 1 (#91 in Table S1) has and (b) event 2 (#82 in Table S1) does not have clear *Pn* depth phases.

different from the catalog (4.3 km; Table S1). Our relative depth is tightly constrained as the misfit doubles if it is varied by ±1 km (Figures 8c and 8d).

Finally, we determine absolute focal depths for these events. Results are averaged if there are multiple master events. Depth uncertainty of these events comes from both the absolute depth uncertainty of the master event and the relative depth uncertainty in the relocation algorithm. It is generally difficult to quantify this

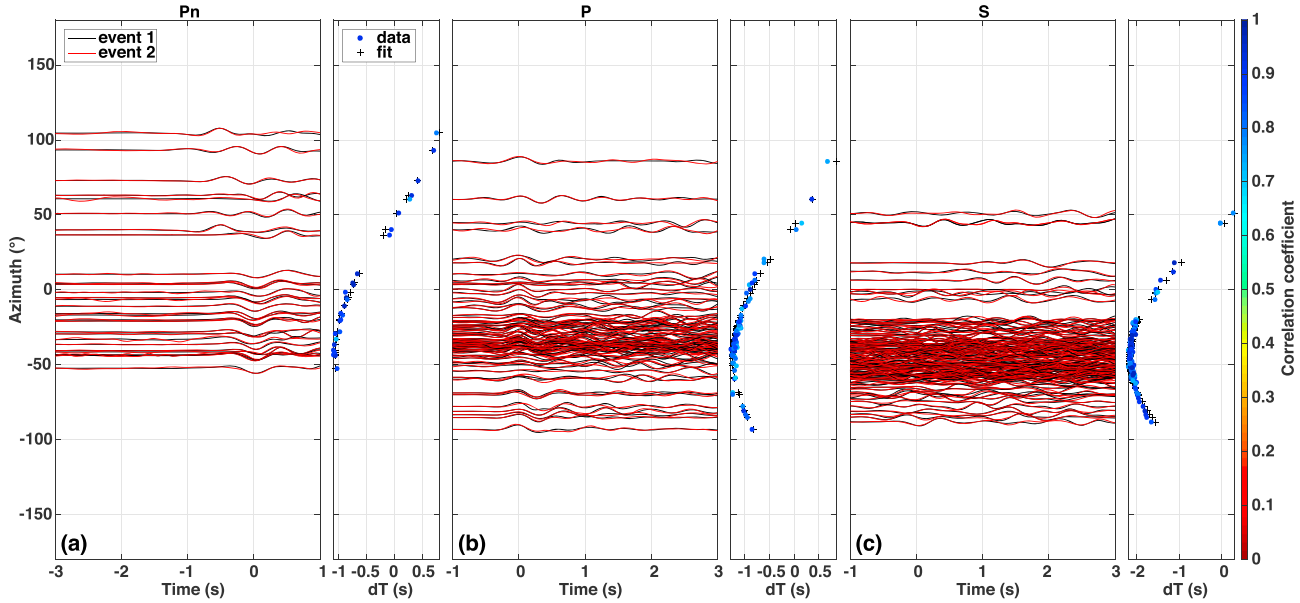

Figure 7. Waveform cross correlation between the event pair in Figure 6 where (a), (b), and (c) are for *Pn*, *P*, and *S* segments, respectively. In (a), (b), and (c), the left panels display waveform comparison between event 1 and event 2 (after alignment). The right panels show the measured differential travel times (circles; color-coded by the cross-correlation coefficient) and their best fits (black crosses). The latter are determined using a grid search algorithm as illustrated in Figure 8.

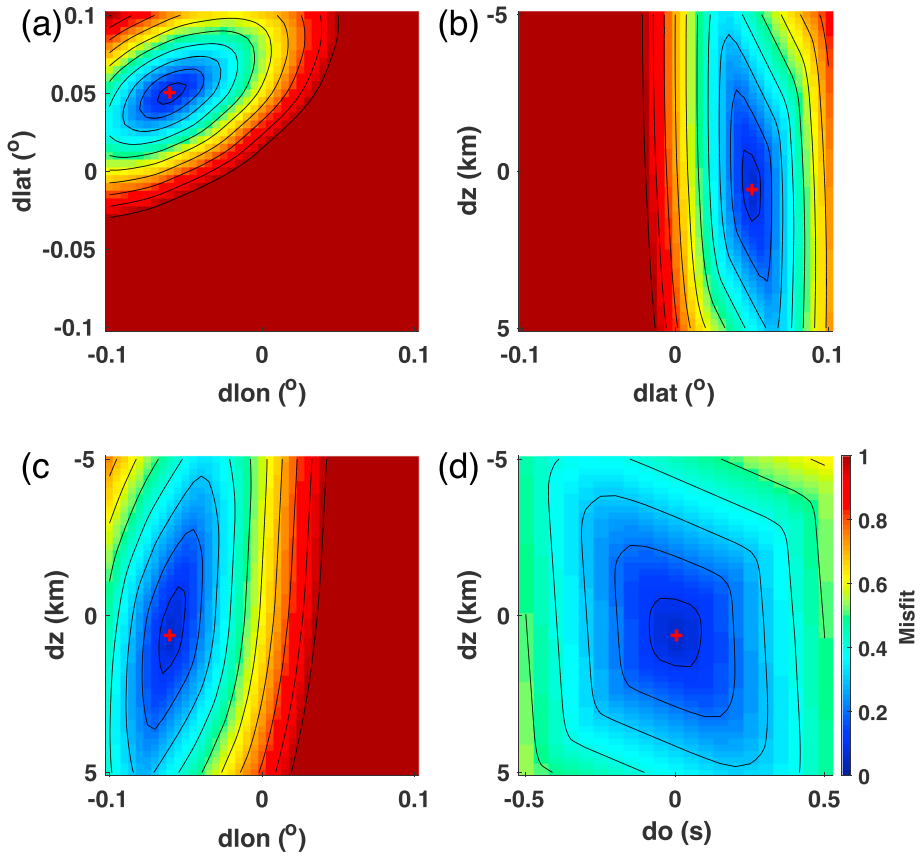

Figure 8. Grid search of relative locations and differential origin time between the event pair in Figure 6 (event 1 with respect to event 2). Colors show the misfit of average differential travel times in (a) map view and along the (b) south-north and (c) west-east vertical cross sections, and (d) shows the tradeoff between relative depth and differential origin time (reduced by the catalog origin time difference).

composite depth uncertainty. A typical value of absolute depth uncertainty is ~1 km for events determined with the relative location method. Our relative horizontal locations are consistent with the relocated catalog of SCSN (Hauksson et al., 2012).

3. Results

We determine focal depths of 93 events out of 122 $M \geq 4.0$ earthquakes in the 2010 El Mayor-Cucapah sequence (Table S1). The rest events are mostly early aftershocks of the main shock (supporting information Figure S4) and thus have a low signal-to-noise ratio. Among the 93 events, 36 have their focal depths determined by *Pn* depth phase modeling (supporting information Figure S3). These events are classified as group A. A total of 57 events have their focal depths determined with the relative location method. We assign them to groups B and C, based on the visual check of their reliability, including data azimuthal coverage, cross-correlation coefficients, misfit values, and depth uncertainties. Generally, events in groups A and B have well determined focal depths (uncertainty with less than about 1 km), and events in group C have relatively larger depth uncertainty. We also attempt to validate our focal depth estimation using teleseismic *P* waveforms. However, only the largest magnitude aftershock (#104 in Table S1, $M = 5.72$) shows relatively clear teleseismic *P* wave and depth phases. Waveform modeling suggests a focal depth of ~8 km, consistent with our result in Table S1 (supporting information Figure S5).

Our earthquake focal depths are more tightly clustered compared with SCSN catalog depths. The events are mainly confined to the depth range between 3 and 10 km, with a peak at ~6 km (Figure 9; Table S1). In

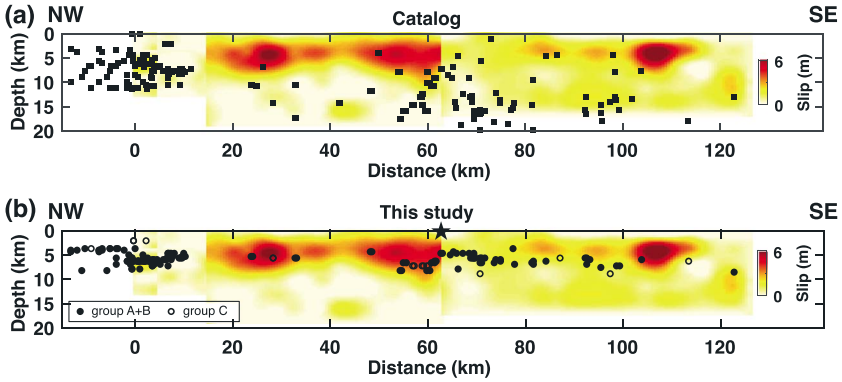

Figure 9. Depth distribution of the 2010 El Mayor-Cucapah earthquake sequence from (a) the SCSN catalog (Hauksson et al., 2012) and (b) this study. The background image shows the inverted coseismic slip of the main shock (Wei et al., 2011). Black star marks the epicenter of the main shock. Depth uncertainty of seismicity in groups A and B is about 1 km.

contrast to the SCSN catalog, we find no systematic difference in earthquake depth between the event cluster near the Yuha Desert and that near the hypocenter of the main shock.

Lateral variation in earthquake depth is observed in each cluster. A change in seismicity depth is observed at the northern tip of the coseismic rupture zone (Figure 9). Most events within the coseismic rupture region are located at a depth of ~6 km. Across the northern tip of the rupture, in the Yuha Desert, however, seismicity is shifted to both shallower and deeper depths at ~4 and ~8 km, respectively. Such change in earthquake depth distribution is likely due to the complex faulting in the Yuha Desert where conjugate faults trending northwest and northeast are both active (Isaac, 1987; Kroll et al., 2013). Overall, our earthquake depth distribution is similar to that located using data from both the SCSN and a dense temporary seismic network (Kroll et al., 2013; Ross et al., 2017). Seismicity tends to become shallower toward the epicenter of the main shock, where an extensional fault meets the two oppositely dipping mainshock faults (Figure 9). The change in seismicity depth is laterally continuous.

4. Discussion

Aftershocks are mainly located outside of coseismic high-slip patches of the 2010 El Mayor-Cucapah earthquake. The anticorrelation between coseismic slip and aftershock distribution was noticed by Wei et al. (2011) and observed in many other regions (e.g., Das & Henry, 2003; Hsu et al., 2006; Yagi et al., 2001). Moreover, our results show that aftershocks also tend to occur near the lower terminus of high slip patches, especially near the epicenter of the main shock (Figure 9). Wei et al. (2011) interpreted the spatial anticorrelation as a result of residual strain releasing adjacent to high slip patches of the main shock. It is also likely that aftershocks were caused by local stress concentration near high slip patches (e.g., Shen et al., 2009) or driven by postseismic slip (e.g., Hsu et al., 2006).

The maximum focal depth of $M \geq 4.0$ events is ~10 km. Although we cannot fully preclude the existence of deeper events with smaller magnitude, it is most likely that the seismogenic depth in this region is only about 10 km. Previous studies also revealed a similar shallow seismogenic depth in the northern part of the study zone, where earthquake depth is relatively well constrained (Hauksson et al., 2012; Kroll et al., 2013; Ross et al., 2017) or in the northern Imperial Valley region (Doser & Kanamori, 1986). Magistrale and Rockwell (1996) found a southward shallowing of seismogenic depth from 17 km in the central Elsinore Fault to 10 km in the southern Elsinore Fault. The relatively shallow seismogenic depth is consistent with high surface heat flow in the Imperial Valley and adjacent areas (Lachenbruch et al., 1985), although it can be affected by other factors such as strain rate and lithology (Magistrale, 2002). Assuming a nominal thermal conductivity of 2–2.5 $W \cdot m^{-1} \cdot K^{-1}$ for the upper crust (Bonner et al., 2003), the heat flow in the Imperial Valley (~100 mW/m^2) predicts a 450 ± 50 °C geotherm at the base of the seismogenic zone, similar to other regions in Southern California (Bonner et al., 2003).

Previous studies suggest similar seismotectonic characteristics between the 2010 El Mayor-Cucapah earthquake sequence and other two M7.0+ earthquake sequences in southern California—the 1992 M_w 7.3 Landers and the 1999 M_w 7.1 Hector Mine earthquake sequences (Hauksson et al., 2011). All of them occurred on multiple fault segments that are off the main Pacific-North America plate boundary. Our relocated focal depth further confirms this conclusion, as the seismogenic depth of the 2010 El Mayor-Cucapah earthquake sequence is similar to that of the other two (Hauksson et al., 1993, 2002).

Regional depth phases are known to be effective in constraining earthquake depth, but they are not routinely analyzed. One of the main challenges lies in the complexity of regional/local waveforms. Following the first arrival, there are many phases associated with crustal reverberations and mode conversions. Multipathing and seismic scatterings due to 3-D heterogeneous structures make phase identification even more difficult. Although theoretically one station at a proper distance range is enough to determine the earthquake depth, it potentially faces the problem of phase misidentification. Our array processing technique, which extracts coherent signals from a set of stations within a narrow azimuthal range, is thus an efficient way to facilitate depth phase identification. The method can potentially be applied to other regions with both regional seismicity and relatively dense station coverage. It may also be extended to smaller magnitude events to examine a more complete set of regional seismicity.

5. Conclusions

Our study uses both high-frequency regional depth phase modeling and a relative relocation method to provide constraints on the depth distribution of the 2010 El Mayor-Cucapah earthquake sequence. We apply array analysis to help identify *Pn* depth phases as well as increase their signal-to-noise ratio. For events without clear *Pn* depth phases, we relocate their depths with respect to nearby master events using differential travel times of *Pn*, *P*, and *S*. In total, we determine focal depths of 93 out of 122 $M \geq 4.0$ events in the 2010 El Mayor-Cucapah earthquake sequence. These events are clustered in the depth range of 3–10 km, suggesting a relatively shallow seismogenic zone. Most of our relocated events are located either in the gap of large coseismic rupture patches or near their lower terminus, which may be caused by residual strains, local stress concentration, or postseismic slip.

Data and Resources

Event catalogs investigated in this study were obtained from the Southern California Earthquake Data Center (SCEDC) at Caltech (http://scedc.caltech.edu/eq-catalogs, last accessed Oct, 2018). Broadband waveforms were retrieved from SCEDC and the Incorporated Research Institutions for Seismology (IRIS) Data Management Center (https://ds.iris.edu/ds/nodes/dmc/, last accessed October 2018).

Acknowledgments

We appreciate the constructive review by S. Ni and an anonymous reviewer. Comments from Rob Graves and Sarah Minson helped improve the quality of this manuscript. We thank Shengji Wei for the coseismic rupture model of 2010 El Mayor-Cucapah earthquake. This research was supported by USGS/NEHRP grants G16AP00147 and G18AP00028 and by the Southern California Earthquake Center (SCEC) (award 17044), which is funded by NSF Cooperative Agreement EAR-1033462 and USGS Cooperative Agreement G12AC20038. C. Y and Z. Z are partially supported by National Science Foundation NSF grants 1722879 and 1829496. We used GMT from Wessel et al. (2013) to make Figure 1. We used waveforms and parametric data from the Caltech/USGS Southern California Seismic Network (SCSN), doi:10.7914/SN/CI, stored at the Southern California Earthquake Data Center, doi:10.7909/C3WD3xH1.

References

Bonner, J. L., Blackwell, D. D., & Herrin, E. T. (2003). Thermal constraints on earthquake depths in California. *Bulletin of the Seismological Society of America*, *93*(6), 2333–2354. https://doi.org/10.1785/0120030041

Brudzinski, M. R., Thurber, C. H., Hacker, B. R., & Engdahl, E. R. (2007). Global prevalence of double Benioff zones. *Science*, *316*(5830), 1472–1474. https://doi.org/10.1126/science.1139204

Chen, W., & Molnar, P. (1983). Focal depths of intracontinental and intraplate earthquakes and their implications for the thermal and mechanical properties of the lithosphere. *Journal of Geophysical Research*, *88*(B5), 4183–4214. https://doi.org/10.1029/JB088iB05p04183

Craig, T. J., & Heyburn, R. (2015). An enigmatic earthquake in the continental mantle lithosphere of stable North America, Earth Planet. *Science Letters*, *425*, 12–23. https://doi.org/10.1016/j.epsl.2015.05.048

Das, S., & Henry, C. (2003). Spatial relation between main earthquake slip and its aftershock distribution. *Reviews of Geophysics*, *41*(3), 1013. https://doi.org/10.1029/2002RG000119

Doser, D. I., & Kanamori, H. (1986). Depth of seismicity in the Imperial Valley Region (1977–1983) and its relationship to heat flow, crustal structure and the October 15, 1979, earthquake. *Journal of Geophysical Research*, *91*(B1), 675. https://doi.org/10.1029/JB091iB01p00675

Ekström, G., Nettles, M., & Dziewoński, A. (2012). The global CMT project 2004–2010: Centroid-moment tensors for 13,017 earthquakes. *Physics of the Earth and Planetary Interiors*, *200-201*, 1–9. https://doi.org/10.1016/j.pepi.2012.04.002

Engdahl, E., van der Hilst, R., & Buland, R. (1998). Global teleseismic earthquake relocation with improved travel times and procedures for depth determination. *Bulletin of the Seismological Society of America*, *88*(3), 722–743.

Fletcher, J. M., Teran, O. J., Rockwell, T. K., Oskin, M. E., Hudnut, K. W., Mueller, K. J., et al. (2014). Assembly of a large earthquake from a complex fault system: Surface rupture kinematics of the 4 April 2010 El Mayor–Cucapah (Mexico) M_w 7.2 earthquake. *Geosphere*, *10*(4), 797–827. https://doi.org/10.1130/GES00933.1

Gomberg, J. S., Shedlock, K. M., & Roecker, S. W. (1990). The effect of *S*-wave arrival times on the accuracy of hypocenter estimation. *Bulletin of the Seismological Society of America*, *80*(6A), 1605–1628.

Han, L., Hole, J. A., Stock, J. M., Fuis, G. S., Williams, C. F., Delph, J. R., et al. (2016). Seismic imaging of the metamorphism of young sediment into new crystalline crust in the actively rifting Imperial Valley, California. *Geochemistry, Geophysics, Geosystems*, *17*, 4566–4584. https://doi.org/10.1002/2016GC006610

Hauksson, E. (2000). Crustal structure and seismicity distribution adjacent to the Pacific and North America plate boundary in southern California. *Journal of Geophysical Research*, *105*(B6), 13,875–13,903. https://doi.org/10.1029/2000JB900016

Hauksson, E., Jones, L. M., & Hutton, K. (2002). The 1999 M_w 7.1 Hector Mine, California, earthquake sequence: Complex conjugate strike-slip faulting. *Bulletin of the Seismological Society of America*, *92*(4), 1154–1170. https://doi.org/10.1785/0120000920

Hauksson, E., Jones, L. M., Hutton, K., & Eberhart-Phillips, D. (1993). The 1992 Landers earthquake sequence: Seismological observations. *Journal of Geophysical Research*, *98*(B11), 19,835–19,858. https://doi.org/10.1029/93JB02384

Hauksson, E., Stock, J., Hutton, K., Yang, W., Vidal-Villegas, J. A., & Kanamori, H. (2011). The 2010 M_w 7.2 El Mayor-Cucapah earthquake sequence, Baja California, Mexico and Southernmost California, USA: Active seismotectonics along the Mexican Pacific Margin. *Pure and Applied Geophysics*, *168*(8–9), 1255–1277. https://doi.org/10.1007/s00024-010-0209-7

Hauksson, E., Yang, W., & Shearer, P. M. (2012). Waveform relocated earthquake catalog for southern California (1981 to June 2011). *Bulletin of the Seismological Society of America*, *102*(5), 2239–2244. https://doi.org/10.1785/0120120010

Helmberger, D., & Engen, G. (1980). Modeling the long-period body waves from shallow earthquakes at regional ranges. *Bulletin of the Seismological Society of America*, *70*(5), 1699–1714.

Helmberger, D., Stead, R., Ho-Liu, P., & Dreger, D. (1992). Broadband modelling of regional seismograms: Imperial Valley to Pasadena. *Geophysical Journal International*, *110*(1), 42–54. https://doi.org/10.1111/j.1365-246X.1992.tb00711.x

Hsu, Y.-J., Simons, M., Avouac, J.-P., Galetzka, J., Sieh, K., Chlieh, M., et al. (2006). Frictional afterslip following the 2005 Nias-Simeulue earthquake, Sumatra. *Science*, *312*(5782), 1921–1926. https://doi.org/10.1126/science.1126960

Husebye, E. S., Matveeva, T., & Fedorenko, Y. V. (2013). Focal-depth estimation using Pn-Coda phases including *pP*, *sP*, and *PmP*. *Bulletin of the Seismological Society of America*, *103*(3), 1771–1783. https://doi.org/10.1785/0120120015

Isaac, S., 1987, Geology and structure of the Yuha Desert between Ocotillo, California, USA and Laguna Salada, Baja California, Mexico, PhD thesis, San Diego State University.

Jia, Z., Ni, S., Chu, R., & Zhan, Z. (2017). Joint inversion for earthquake depths using local waveforms and amplitude spectra of Rayleigh waves. *Pure and Applied Geophysics*, *174*(1), 261–277. https://doi.org/10.1007/s00024-016-1373-1

Kafka, A. L. (1990). *Rg* as a depth discriminant for earthquakes and explosions: A case study in New England. *Bulletin of the Seismological Society of America*, *80*(2), 373–394.

Kroll, K. A., Cochran, E. S., Richards-Dinger, K. B., & Sumy, D. F. (2013). Aftershocks of the 2010 M_w 7.2 El Mayor-Cucapah earthquake reveal complex faulting in the Yuha Desert, California. *Journal of Geophysical Research: Solid Earth*, *118*, 6146–6164. https://doi.org/10.1002/2013JB010529

Lachenbruch, A. H., Sass, J., & Galanis, S. Jr. (1985). Heat flow in southernmost California and the origin of the Salton Trough. *Journal of Geophysical Research*, *90*(B8), 6709–6736. https://doi.org/10.1029/JB090iB08p06709

Langston, C. A. (1987). Depth of faulting during the 1968 Meckering, Australia, earthquake sequence determined from waveform analysis of local seismograms. *Journal of Geophysical Research*, *92*(B11), 11,561–11,574. https://doi.org/10.1029/JB092iB11p11561

Lee, E., Chen, P., Jordan, T. H., Maechling, P. B., Denolle, M. A., & Beroza, G. C. (2014). Full-3-D tomography for crustal structure in southern California based on the scattering-integral and the adjoint-wavefield methods. *Journal of Geophysical Research: Solid Earth*, *119*, 6421–6451. https://doi.org/10.1002/2014JB011346

Lui, S. K. Y., Helmberger, D., Yu, J., & Wei, S. (2016). Rapid assessment of earthquake source characteristics. *Bulletin of the Seismological Society of America*, *106*(6), 2490–2499. https://doi.org/10.1785/0120160112

Ma, S. (2010). Focal depth determination for moderate and small earthquakes by modeling regional depth phases *sPg*, *sPmP*, and *sPn*. *Bulletin of the Seismological Society of America*, *100*(3), 1073–1088. https://doi.org/10.1785/0120090103

Magistrale, H. (2002). Relative contributions of crustal temperature and composition to controlling the depth of earthquakes in southern California. *Geophysical Research Letters*, *29*(10), 1447. https://doi.org/10.1029/2001GL014375

Magistrale, H., & Rockwell, T. (1996). The central and southern Elsinore Fault Zone, Southern California. *Bulletin of the Seismological Society of America*, *11*, 1793–1803.

Mori, J. (1991). Estimates of velocity structure and source depth using multiple *P* waves from aftershocks of the 1987 Elmore Ranch and Superstition Hills, California, earthquakes. *Bulletin of the Seismological Society of America*, *81*(2), 508–523.

Persaud, P., Ma, Y., Stock, J. M., Hole, J. A., Fuis, G. S., & Han, L. (2016). Fault zone characteristics and basin complexity in the southern Salton Trough, California. *Geology*, *44*(9), 747–750. https://doi.org/10.1130/G38033.1

Prieto, G. A., Froment, B., Yu, C., Poli, P., & Abercrombie, R. (2017). Earthquake rupture below the brittle-ductile transition in continental lithospheric mantle. *Science Advances*, *3*(3), e1602642. https://doi.org/10.1126/sciadv.1602642

Ross, Z., Rollins, C., Cochran, E. S., Hauksson, E., Avouac, J., & Ben-Zion, Y. (2017). Aftershocks driven by afterslip and fluid pressure sweeping through a fault-fracture mesh. *Geophysical Research Letters*, *44*, 8260–8267. https://doi.org/10.1002/2017GL074634

Shearer, P. M. (1997). Improving local earthquake locations using the *L*1 norm and waveform cross correlation: Application to the Whittier Narrows, California, aftershock sequence. *Journal of Geophysical Research*, *102*(B4), 8269–8283. https://doi.org/10.1029/96JB03228

Shen, Z.-K., Sun, J., Zhang, P., Wan, Y., Wang, M., Bürgmann, R., et al. (2009). Slip maxima at fault junctions and rupturing of barriers during the 2008 Wenchuan earthquake. *Nature Geoscience*, *2*(10), 718–724. https://doi.org/10.1038/ngeo636

Sibson, R. H. (1986). Earthquakes and rock deformation in crustal fault zones. *Annual Review of Earth and Planetary Sciences*, *14*(1), 149–175. https://doi.org/10.1146/annurev.ea.14.050186.001053

Tibi, R., Koper, K. D., Pankow, K. L., & Young, C. J. (2018). Depth discrimination using *Rg*-to-*Sg* spectral amplitude ratios for seismic events in Utah recorded at local distances. *Bulletin of the Seismological Society of America*, *108*(3A), 1355–1368. https://doi.org/10.1785/0120170257

Tsai, Y., & Aki, K. (1970). Precise focal depth determination from amplitude spectra of surface waves. *Journal of Geophysical Research*, *75*(29), 5729–5744. https://doi.org/10.1029/JB075i029p05729

Wang, Z., Chong, J., Ni, S., & Romanowicz, B. (2011). Determination of focal depth by two waveform based methods: A case study for the 2008 Panzhihua earthquake. *Earthquake Science*, *24*(4), 321–328. https://doi.org/10.1007/s11589-011-0794-2

Wei, S., Fielding, E., Leprince, S., Sladen, A., Avouac, J. P., Helmberger, D., et al. (2011). Superficial simplicity of the 2010 El Mayor-Cucapah earthquake of Baja California in Mexico. *Nature Geoscience*, *4*(9), 615–618. https://doi.org/10.1038/ngeo1213

Wessel, P., Smith, W. H. F., Scharroo, R., Luis, J., & Wobbe, F. (2013). Generic mapping tools: Improved version released. *EOS. Transactions of the American Geophysical Union*, *94*(45), 409–410. https://doi.org/10.1002/2013EO450001

Yagi, Y., Kikuchi, M., & Sagiya, T. (2001). Co-seismic slip, post-seismic slip, and aftershocks associated with two large earthquakes in 1996 in Hyuga-nada, Japan. *Earth, Planets and Space*, *53*(8), 793–803. https://doi.org/10.1186/BF03351677

Yu, C., Zhan, Z., Hauksson, E., Cochran, E. S., & Helmberger, D. V. (2019). Determining Moho depth beneath sedimentary basins using regional *Pn* multiples. *Bulletin of the Seismological Society of America*, *109*(3), 1171–1179. https://doi.org/10.1785/0120180325

Zhu, L., & Helmberger, D. V. (1996). Advancement in source estimation techniques using broadband regional seismograms. *Bulletin of the Seismological Society of America*, *86*(5), 1634–1641.

Zhu, L., & Rivera, L. A. (2002). A note on the dynamic and static displacements from a point source in multilayered media. *Geophysical Journal International*, *148*(3), 619–627. https://doi.org/10.1046/j.1365-246X.2002.01610.x

Zonno, G., & Kind, R. (1984). Depth determination of North Italian earthquakes using Grafenberg data. *Bulletin of the Seismological Society of America*, *74*(5), 1645–1659.